PCCP

Accepted Manuscript

ROYAL SOCIETY OF CHEMISTRY

www.rsc.org/pccp

Graphical abstract

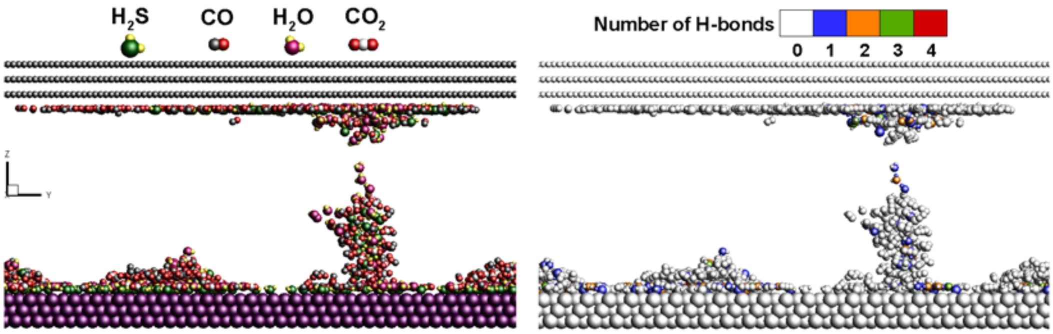

We report a comprehensive molecular adsorption study that allowed us to explore the fundamental separation mechanisms of hydrogen sulfide (H_2S) from acidic gas mixtures inside metal-doped graphite micropores. The figures show the molecular interactions and adsorption conformations of an equimolar fraction of CO_2, H_2O, CO, and H_2S mixtures inside a slit pore at 50 K (left) and the corresponding distribution state of hydrogen bonds at this transient moment (right).

Molecular dynamics investigation of separation of hydrogen sulfide from acidic gas mixtures inside metal-doped graphite micropore

Pei-Hsing Huang

Department of Mechanical Engineering, National Pingtung University of Science and Technology, Pingtung 912, Taiwan, R.O.C.

Abstract The separation of poisonous compounds from various process fluids has long been highly intractable, motivating the present study on the dynamic separation of H_2S in acidic-gas-mixture-filled micropores. The molecular dynamics approach coupled with the isothermal-isochoric ensemble was used to model the molecular interactions and adsorption of $H_2S/CO_2/CO/H_2O$ mixtures inside metal-doped graphite slits. Due to the difference of adsorption characteristics between two distinct adsorbent materials, the metal dopant in the graphitic micropores led to competitive adsorption, i.e., the Au and graphite walls compete to capture free adsorbates. The effects of competitive adsorption coupled with changes of gas temperature, concentration, constituent ratio, and slit width on the constituent separation of mixtures were systematically studied. The molecule-wall binding energies calculated in this work (those of H_2S, H_2O, and CO on Au walls and those of H_2O, CO, and CO_2 on graphite walls) show good agreement with those obtained using density functional theory (DFT) and experiment results. The z-directional self-diffusivities (D_z) for adsorbates inside the slit ranged from 10^{-9} to 10^{-7} $m^2 \cdot s^{-1}$ as the temperature was increased from 10 to 500 K. The values are comparable with a typical microporous fluid (10^{-8}~10^{-9} $m^2 \cdot s^{-1}$ in a condensed phase and 10^{-6}~10^{-7} $m^2 \cdot s^{-1}$ in the gaseous state). The formation of H-bonding networks and hydrates of H_2S is disadvantageous for the separation of mixtures. The results indicate that H_2S can be efficiently separated from acidic gas mixtures onto the Au(111) surface by (i) reducing the mole fraction of H_2S and H_2O in the mixtures, (ii) raising the gas temperature to the high temperature limit (≥ 400 K), and (iii) lowering the slit width to below the threshold dimension (≤ 23.26 Å).

---

*Corresponding author. E-mail address: phh@mail.npust.edu.tw (P.-H. Huang)

1. Introduction

Hydrogen sulfide (H_2S) is a toxic, acidic compound found in natural gas, crude petroleum, volcanic gases, and emissions from various coal-fired and petrochemical industrial plants[1-3]. H_2S has many detrimental effects that can lead to industrial corrosions[4-7], the formation of hydrate blockage in pipeline[8,9], as well as oxidation to sulfur oxide, a major source of acid rain[5]. Exposure to > 100 ppm H_2S can even threaten human life[10]. Recent studies have revealed that H_2S is an important regulatory mediator and neurotransmitter in the human body[11-12]. A deficiency of H_2S is closely related to central-nervous-system-related diseases (including Alzheimer’s and Parkinson’s diseases[11,12]). Although a trace amount of H_2S is vital to the human body, the removal of H_2S from various process fluids is of importance due to its high toxicity and corrosion, as well as the restrictive emission standards are worldwide enforced[5,13].

Due to the high toxicity and inflammability of H_2S, its adsorption properties have rarely been subjected to systematic empirical research. Xiao *et al.*[1,5] investigated the effects of impregnation, relative humidity, temperature, and concentration on the catalysis and adsorption of H_2S using unmodified activated carbon (AC) and sodium-carbonate-impregnated AC (IAC). Compared to the unmodified AC, IAC exhibited more than three-fold higher adsorption capability for H_2S under dry conditions[1]. Cal *et al.*[7] used various ACs as adsorbents to examine the effects of Zn impregnation and gas composition on H_2S removal from coal gasification processes. They found that metal-based sorbents are effectual at around 550 °C, but lose much of their capability at lower gas reaction temperatures. In contrast, carbon-based sorbents retain their activity at low reaction temperatures[7]. Leavitt and Beebe[14] investigated H_2S adsorbed on a clean Au(111) surface using temperature-programmed desorption and X-ray photoelectron spectroscopy. They observed that H_2S only bound weakly to the Au(111) surface with a Redhead desorption energy of 9.8 ± 0.2

kcal·mol^{-1} at 165 K[14]. Aside from these experimental reports, a few theoretical studies have been conducted on H_2S adsorption properties. Faure *et al.*[15] investigated the solubility and self-diffusion of CO_2 and H_2S in polyethylene melts at 433 K and pressures in the range of 0.1-10 MPa using Monte Carlo (MC) simulations. Hellmann *et al.*[16] proposed a six-dimensional potential energy hyper-surface for predicting the thermophysical properties of H_2S based on quantum-mechanical methods. Using *ab* initio calculations, Sellers[17] estimated the binding energy of H_2S to the Au(111) surface to be 9.4 kcal/mol. Vorholz *et al.*[18] predicted the vapor-liquid phase equilibrium of H_2S and the H_2O-H_2S binary system based on MC simulations.

The presence of vacancy defects alters the electronic structure in graphene,[19] which undoubtedly enhances the adsorption properties. The vacancy defects with unsaturated dangling bonds are able to capture adsorbates effectively through charge transfer or covalent bonds with high adsorption energy. Defective graphene is useful for adsorbing specific molecules as a means of promoting the sensitivity and selectivity of graphene-based sensors.[19] However, strong chemisorptions via a defective graphene are disadvantageous to the desorption of adsorbed molecules and the regeneration of adsorbents. The metal-organic framework (MOF) is an emerging class of porous materials, the structure of which comprises metal-oxides joined by organic ligand linkers to form micropore adsorbents. Britt *et al.*[20] demonstrated the effectiveness of MOFs in the removal of gases that are troublesome for AC, such as ammonia and ethylene oxide. However, CO cannot be captured by any of the MOFs. Molecular sieving membranes can also be used for the separation of various harmful gases. Lu et al.[21] demonstrated that nitrogen-doping of a porous graphene membrane can significantly enhance selectivity in the separation of O_2 from a variety of harmful gases. They observed a considerable reduction in the diffusion barrier for O_2 across the monolayer membrane due to a weakening in the overlap of atomic electron density at pores resulting from N substitution. Metal-impregnated porous carbons are viewed as one of the more efficient, renewable, and economical adsorbents, among the MOFs and molecular sieving materials that are currently available. Metal-impregnated porous carbons are particularly noteworthy for their ability to retain structural stability at elevated temperatures.

It is known that fluids confined in molecular-level micropores can exhibit physical behaviors that are quite different from those of their bulk counterparts, e.g., diffusion[22-26], viscosity[24,26], capillarity[24,25], and phase changes[24,26,27]. Understanding the underlying mechanisms of the fluid confinement behaviors can guide the design of novel adsorption materials for capturing particular molecules. Selective adsorption and competitive adsorption in microporous adsorbents are two important mechanisms, affecting the adsorption scenario and the efficacy of the overall adsorption system. By regulating the factors related to these two adsorption mechanisms, one can substantially enhance the adsorption capacity by one or two orders of magnitude[23,28]. These sorption-related factors can be classified into several major facets, including interactions between fluid molecules (e.g., diffusivity ratio[29], hydration state[8,9,23], polarization[3,9], and H-bonding[30,31]), surface properties of the adsorbent material (e.g., doping[9,32], impregnated[1,5,7,13], activated[1,2,5,7], pH[33,34], and hydrophilic/hydrophobic[35,36]), thermodynamic properties of the fluid (e.g., concentration[8,9,13], constituent[7,23,33], viscosity[24,26], temperature[25-27], and pressure[8,9,15,27]), and micropore conformation (e.g., pore size distribution[22-25,28] and shape[11,23,25,32]). These factors have been demonstrated to have considerable impacts on the adsorption kinetics and fluid transport properties in a microporous adsorption system. Since such miniature systems are crucial for various applications (e.g., waste oil treatment, biogas recovery, membrane separation, and purification)[28,37], it is expected to establish a comprehensive molecular model so as for predicting molecular-level sorption behaviors.

Since harmful gas emissions are detrimental to human health and their elimination consumes many resources, the development of more efficient, recyclable, and cost-effective adsorbent is imperative. The present work investigates the adsorption trends and separation of hydrogen sulfide from multi-component acidic gas mixtures inside a slit pore using fully atomistic molecular dynamics (MD) simulations. Experimental research[7,38,39] has demonstrated that metal dopants can be used to enhance the ability of carbon adsorbents to remove harmful matters through the formation of surface complexes or strong physical adsorption. Porous carbon adsorbents possess a large surface area and pore volume, which are characteristics high beneficial to metallic impregnation[38]. Differences in the adsorption characteristics between impregnated metals and the primitive carbon adsorbent in the micropores can lead to competitive adsorption; i.e., the metal and carbon walls compete to capture free adsorbates. This characteristic makes metal-impregnated microporous carbon a promising adsorbent for the separation of specific molecules from mixtures. For a physical model in this study, we adopted micropores with a slit configuration comprising a metal wall on one side (to imitate a metal-impregnated surface) and a Gr wall on the other side to gain a better understanding of the effects of metal additives on the constituent separation and adsorption behaviors. To explore the effects of metal additives on the constituent separation and fluid confinement behaviors, gold (Au) and graphite (Gr) slit walls are adopted in simulations. The Au(111) surface is considered due to its chemical stability and extensive experimental data. The acidic gas mixtures comprise hydrogen sulfide, carbon dioxide, carbon monoxide, and water vapor, which commonly appear in transmission pipelines and reservoirs in the fossil fuel and natural gas industries. For determining the effect of composition on adsorption behaviors, acidic gas mixtures with various constituent ratios and molar concentrations were systematically examined. The areas of focus in this study were (i) the dynamic diffusion and confinement behaviors of pure H_2S, CO_2, CO, and H_2O and their mixtures inside slit pores, (ii) the effect of competitive adsorption on the separation of multi-component mixtures, i.e., two distinct adsorbent materials (i.e., Au and Gr) competing to capture free adsorbates, (iii) how to enhance the feasibility of fluid separation from a multi-component mixture via regulation of sorption-related parameters, and (iv) the influence of the formation of hydrates and H-bonding networks between hydrogen sulfide and water molecules on adsorption properties.

2. Models and Computational Methods

The dynamics properties and adsorption trends of hydrogen sulfide, oxocarbons, and water mixtures inside the Au(111)/Gr slit pore were investigated using isothermal-isochoric (NVT ensemble) MD simulations. For ensuring that the simulations were sufficiently close to realistic scenarios, four potential energy models, namely energy calculation and dynamics (ENCAD) [40,41], Spohr potential function[42,43], Dreiding force field[44,45], and the Lennard-Jones (L-J) model integrated Coulomb pair potentials[36,46-49] were adopted in the present study. ENCAD was used for modeling the adsorbate molecules. This model can accurately construct molecular structures based on the X-ray and neutron diffractions and can derive thermodynamic properties corresponding with those obtained from experimental data[40]. Here, a brief introduction of the ENCAD model is given to make the computational process more explicit and complete. The ENCAD energy function used here is as follows:

$$U_{ENCAD} = \sum_{i}^{stretching\,bonds} \frac{1}{2}k_b^i(b_i - b_0^i)^2 + \sum_{i}^{bending\,bonds} \frac{1}{2}k_\theta^i(\theta_i - \theta_0^i)^2 + \sum_{nonbonded\;pairs} [A_{SC}\varepsilon(\frac{r_0}{r_{ij}})^{12} - 2\varepsilon(\frac{r_0}{r_{ij}})^6 - S_{vdw}^A(r_{ij})] + \sum_{pairs} 332[q^i q^j / r_{ij} - S_{els}^A(r_{ij})] \quad (1)$$

The first two terms in Eq. (1) depict the potential energies respectively related to the extending and bending of covalent bonds associated with adsorbate molecules. k_b^i and k_θ^i are force constants of the stretching and bending of the *i*th bond, respectively; b_i, θ_i, b_0^i, and θ_0^i are the energy parameters of the bond length, the bending angle, the equilibrium length of the bond, and the equilibrium angle of the bending angle, respectively.[23] The energy parameters used for describing the stretching and bending of covalent bonds are listed in Table 1. The last two terms in Eq. (1) represent the van der Waals (vdW) and electrostatic energies, respectively, which describe the nonbonded interactions between pairs of atoms separated by different molecules or covalent structures.[23] The parameter A_{sc} with the value of 0.84 in Eq. (1) is a scale factor used for compensation of the reduced attraction caused by the truncation of potential energy.[23] q^i and q^j are the atomic partial charges of two interactive molecules. The terms $S^A_{vdw}(r_{ij})$ and $S^A_{els}(r_{ij})$ in Eq. (1) represent the truncation shift functions of the vdW and electrostatic energies, respectively. The general form of the truncation shift function can be expressed as follows[37]:

$$S^A_f(r) = \begin{cases} [f(r_{c1}) + (r - r_{c1})(df(r_{c1})/dr)] & for\ r \le r_{c1} \\ 0 & for\ r > r_{c1} \end{cases} \tag{2}$$

where $f(r_{c1})$ and r_{c1} represent the energy function and the truncation distance, respectively. Accordingly, the complete forms of the energy function $S^A_{vdw}(r_{ij})$ and $S^A_{els}(r_{ij})$ can refer to Ref. 23. The cutoff length r_{c1}= 6 Å was adopted for the computation of the truncation shift function, $S^A_f(r)$, in Eq (2). This value was proposed by the original ENCAD potential energy[40] and the F3C water model[41]. When $r > r_{c1}$, the $S^A_f(r)$= 0, which means that the terms $S^A_{vdw}(r_{ij})$ and $S^A_{els}(r_{ij})$ in Eq. (1) are equal to zero. It should be noted that Eq. (1) includes two other nonbonded interaction terms to describe the long-range van der Waals and electrostatic interactions, $A_{sc}\varepsilon(r_o/r_{ij})^{12} - 2\varepsilon(r_o/r_{ij})^6$ and $332(q^i q^j/r_{ij})$. All of the nonbonded interactions between the various homo- and hetero-molecular pairs in the present work were treated in exactly the same manner using a large truncation radius (r_c=15 Å). Many previous works[22,35,36] have demonstrated that simulations carried out using different water models (e.g., TIP3P, TIP4P, and the simple point charge/extended (SPC/E) model) would yield different adsorption conformations and wetting behaviors in water clusters adsorbed on a GR surface. TIP3P, TIP4P, and SPC/E are rigid water models with fixed bond length and angle.[36,50] To improve the lack of a tetrahedral water structure in TIP3P, a negative interaction center off of the oxygen atom is added in the TIP4P (four-point water model).[41] The TIP4P model is able to reproduce heat capacity corresponding precisely to the experimental results; however, it provides excessive diffusivity at room temperature.[41] The lack of internal flexibility in these rigid water models may result in unrealistic elastic collisions between molecule-molecule and molecule-wall. Therefore, a flexible three-centered (F3C) water model based on the ENCAD potential was adopted. The potential parameters used for the F3C model[41] are given in Table 2. In order to make the computation more efficient and to have longer molecular simulation trajectories, simple potentials based on the L-J integrated Coulomb pair potentials with a large truncation radius (r_c=15 Å) were used to model the nonbonded interactions between different adsorbate molecules and the Gr walls. The nonbonded interaction energy between two interacting atoms i and j separated by an interatomic distance r_{ij} can be expressed as:

$$U_{nonbonded} = \sum_{i,j\ pairs}^{n_s} \frac{q_i q_j}{r_{ij}} + \sum_{i,j\ pairs}^{n_s} 4\varepsilon_{ij}[(\frac{\sigma_{ij}}{r_{ij}})^{12} - (\frac{\sigma_{ij}}{r_{ij}})^{6})] \tag{3}$$

The two right-hand side terms in Eq. (3) describe the long-range electrostatic potentials and the short-range nonpolar interactions (comprising dispersion and repulsion), respectively. n_s is the number of nonbonding atomic pairs within the truncation radius. The potential parameters for the homo-molecular pairs in Eq. (3) are summarized in Table 3. As for the interactions between pairs of hetero-molecules, the effective values of σ and ε can be obtained from those for the homo-molecular pairs using the Lorentz-Berthelot mixing rules.[23]

The water molecule interaction with the Au(111) surface was modeled using the modified Spohr potential energy developed by Dou *et al.*[43]. The complete form of the potential function is:

$$U_{water-Au(111)} = U_{O-Au}(r_{O-Au}) + U_{H1-Au}(r_{H1-Au}) + U_{H2-Au}(r_{H2-Au}) \tag{4}$$

where $U_{O\text{-}Au}$ and $U_{H\text{-}Au}$ are the oxygen- and hydrogen-Au(111) interactions, respectively. They are expressed as follows:

$$U_{O-Au}(r) = D_0\left[\exp(-2\beta_O(r-r_{e1})) - 2\exp(-\beta_O(r-r_{e1}))\right]\cdot S_s(r) \tag{5}$$

$$U_{H-Au}(r) = \lambda D_0 \exp(-2\beta_H(r-r_{e2})) \tag{6}$$

where the switch function S_s has the form[43]:

$$S_s(r) = \begin{cases} 1.0 & , \quad r \le r_{on} \\ \dfrac{(r_{off}^2 - r^2)^2 \cdot (r_{off}^2 + 2r^2 - 3r_{on}^2)}{(r_{off}^2 - r_{on}^2)^3} & , \quad r_{on} < r \le r_{off} \end{cases} \tag{7}$$

In the modified Spohr function, the value of the energy parameter (D_0) is determined from the experimental results of thermal programmed adsorption[51]. r_{on} and r_{off} denote the distances of switch on and off used in the switch function, respectively. The parametric values of the Spohr function are summarized in Table 4.

The interactions between adsorbate molecules (i.e., H_2S, CO, and CO_2) and the Au surface are modeled using the Dreiding force field[44] developed by Mayo et al. This force field has the following energy function form[45]:

$$E_{ij} = D\left\{(\frac{6}{\xi - 6})\exp[\xi(1-\frac{r_{ij}}{R_0}) - (\frac{\xi}{\xi - 6})(\frac{r_{ij}}{R_0})^{-6}]\right\} \tag{8}$$

where r_{ij} is the distance between atoms, D is the energy barrier, and R_0 denotes the equilibrium distance between adsorbate atoms and the Au surface at the energy minimum state. ξ is a dimensionless constant associated with the curvature or stiffness of the inner repulsive wall[45]. The Dreiding potential parameters are listed in Table 5, which were determined from the calculation results of quantum mechanical geometry and the experimental adsorption energy[14,45].

To enhance the realism of the simulations, adsorbate molecules were distributed uniformly over the slit space prior to simulation. The total simulation time was 1.5 ns (i.e., 3 million computational time steps), which was deemed sufficient because the system was generally able to achieve a state of quasi-equilibrium with regard to adsorption before reaching 1.5 million time steps. The slit pores were given planar dimensions of 115.1 Å × 118.6 Å in the x and y directions, respectively, and a variety of slit widths in the z direction. Specially, we selected slit widths of 11.63, 23.26, 34.89, 46.52, 69.78, and 93.04 Å with the aim of identifying the effects of spatial confinement. The value of slit width is determined as the center-to-center distance of Au and C atoms on opposing Au(111) and Gr surfaces. The Gr layers were given an interlayer space of 3.4 Å with each layer constructed using carbon atoms with a bond length of 1.42 Å prearranged in a planar honeycomb lattice. The metal surface was created along the Au(111) Miller plane, which resulted in a hexagonal close-packed layer with an atomic bond length of 2.885 Å. To imitate an infinite slit surface, the minimum imaging criterion[53] and periodic boundary conditions are employed by duplicating the domain of simulation along the x and y directions. The slit pore accommodates a definite number of gas molecules depending on the simulated molar concentration (0.299 to 3.676 mol/L). For investigating the influences of each constituent on the separations of acidic gas mixtures, various mole fractions of $H_2S/CO/CO_2/H_2O$ mixtures are systematically examined. Before the simulation was executed, atoms are randomly assigned thermal vibration velocities commensurate with the temperature of simulations according to the distribution of Maxwell-Boltzmann function. The system was thermally equilibrated at the expected temperature using the rescaling velocity scheme. Seven system temperatures, ranging from 10 to 500 K, are used in the simulations to identify the thermal effects in gas separation processes. The positions, velocities, and accelerations of atoms, as well as intermolecular forces are calculated and updated in each computational time step, i.e., Δt_{MD} = 0.5 fs. The simulation trajectories are derived using Gear's fifth-order predictor-corrector algorithm[52]. The algorithm has excellent stability and adaptability, and provides a good compromise between accuracy and computational time[53,54].

3. Results and discussion

The molecule-wall interaction energies in Eqs. (3), (4), and (8) are a function of the distance between the adsorbed molecule and both Au and Gr walls. The potential energy fields for isolated H_2S, CO, CO_2, and H_2O molecules inside a slit pore obtained from Eqs. (3), (4), and (8) are shown in Fig. 1 as a function of the molecular position in the slit. As shown, the potential energy curve for each kind of molecule-wall interactions has two distinct minima, adjacent to the Au and Gr walls, respectively. The depth of the potential well can be regarded as the energy of the molecule binding to the wall (E_{b}), while the location of the energy minimum corresponds to the equilibrium distance (r_{e}) between the molecular center and the wall surface. The values of $|E_b|$ and r_{e} obtained in this work are summarized and compared with those from other theoretical and experimental results in Table 6. As shown, the binding energies of H_2S and H_2O adsorbed on Au(111) are higher than those for the Gr surface, whereas those of CO and CO_2 show the opposite trend. The values of $|E_b|$ for H_2S, H_2O, and CO on the Au(111) are calculated to be 40.06, 44.54, and 3.24 kJ/mol, respectively, showing good agreement with the experimental data (i.e., 39.35~41.02 kJ/mol for H_2S[14,17] and 43.89 kJ/mol for H_2O[52]) and the DFT using the generalized gradient approximation (DFT-GGA) calculation (i.e., 3.859 kJ/mol for CO[55]). The $|E_b|$ values for H_2O, CO, and CO_2 adhering on the Gr surface are 11.69, 10.14, and 16.57 kJ/mol, respectively, consistent with the experimenal and DFT coupled cluster (DFT/CC) calculation results given by Rubes *et al.*[56] and Vidali *et al.*[57], respectively.

For thoroughly understanding the adsorption behaviors of the acidic gas mixtures inside the Au(111)/Gr slit pore, individual effects of the constituent gases were investigated. Figure 2 shows the profiles of distribution density for H_2S, H_2O, CO_2, and CO inside the micropore at various temperatures, ranging from 10 to 500 K. To make the curves and insets clear, only two sets of simulation results at a given temperature are shown. The insets in Fig. 2 show the corresponding adsorption conformations for each simulation. As shown in Fig. 2(a), the Gr wall adsorbed more H_2S than did Au(111) at a temperature of 10 K, where H_2S self-assembled as layered crystals on Gr and as a monolayer phase on Au(111). When the temperature was increased to 500 K, the adsorption scenario changed. Most of the H_2S adsorbed on the Au(111) wall, forming a dense monolayer, whereas the Gr wall lost much of its capability to capture H_2S due to weak H_2S-Gr interactions not being able to hold high-kinetic-energy H_2S gases. The H_2O vapor in Fig. 2(b) is in a thin gaseous state; therefore molecules were subjected to long-range weak attractions with other H_2O molecules. These attractive forces are nearly in balance and mutually cancel out due to the uniform (symmetric) distribution of H_2O molecules and the lack of relative molecular motion at 100 K. Under these conditions, the suspended H_2O molecules are first adsorbed to fill the adsorption sites on the Au or Gr surfaces, resulting in the formation of a monolayer. At 500 K, the collisions between molecules of high-kinetic-energy and the walls of the slit could result in the rebounding of molecules from the wall causing the desorption of other molecules. If the simulation were conducted in an open space, the H_2O molecules with high kinetic energy would disperse into the atmosphere. Having the free moving high-kinetic-energy H2O molecules confined within the nanoslit increases the probability of hydrogen bonding between H2O molecules, resulting in the formation of loose gaseous clusters adsorbed on the Gr wall. Figures 2(c)-(d) show that both CO and CO_2 can be well adsorbed on the Gr wall at low temperatures of 10~100 K. Gr also better adsorbed CO_2 than did Au(111) at 500 K. Due to the interactions of London dispersion forces by CO_2 molecules themselves, some suspended CO_2 accumulated as gaseous clusters attached to the Au(111) surface. Of note, when the CO gas temperature exceeded 200 K for Au(111) and 500 K for Gr, the Au(111) and Gr almost failed to capture CO. The reason is as below. Au is considered the most inert metal in the periodic table.[58] An electronic structure with a filled d-band makes Au resistant to acidic corrosion and oxidation, and with lower CO adsorption energy than that of other metals, such as Pt and Ni[55]. In the case of Pt, two d-bands cross the Fermi level alter its chemical stability, such that it adsorbs CO. Moreover, the CO molecules have a small permanent dipole moment and atomic partial charge. They are barely aggregated in a gaseous state and possess a very low boiling point. The graphite layer is electrically neutral (non-polarized). The adsorption of CO on graphite surfaces relies on weak van der Waals interactions. The kinetic energy of CO molecules is sufficient to break the binding force between CO and walls, when the temperature of CO gas exceeds 200 K for Au(111) or 500 K for Gr, which results in desorption.

The self-diffusion coefficient is an important transport property for a fluid molecule spontaneously moving in micropores, closely correlated to the frequency of molecule-surface interactions. The factors affecting molecular diffusion in the present study include interactions between molecules, interactions between molecules and walls, molecular concentration, the molar mass of molecules, and temperature of the gas. Molecular diffusion in the direction normal to the pore walls is more directly affected by the attractions of slits than is motion parallel to the pore walls[23]; therefore, we focused on the process of diffusivity in the z direction (D_z). Figure 3 shows the changes of D_z values as a function of temperature for pure H_2S, CO_2, CO, and H_2O molecules inside the slit pore. The self-diffusivity presented in this study was derived on the basis of Einstein relations;[37,52] i.e., $D_z = \left\langle \left| r_z(t+\tau) - r_z(t) \right|^2 / 2\tau \right\rangle$, where $r_z(t+\tau)$ and $r_z(t)$ are the z positions of a tagged atom at times $t+\tau$ and t, respectively; and the angular bracket denotes the thermodynamic average of an ensemble over multiple time intervals τ. Evaluating the molecular diffusivity of the four adsorbates (H_2S, CO_2, CO, and H_2O) using the same benchmark requires that this be performed prior to the adsorption of the molecules (because molecules are commonly immobilized when adsorbed on walls). As shown in Fig. 3, the D_z values of pure H_2S, CO_2, CO, and H_2O inside the slit increased approximately two orders of magnitude, i.e., from 10^{-9} to 10^{-7} $m^2 \cdot s^{-1}$, as the temperature was increased from 10 to 500 K. The values are comparable with those for a typical microporous fluid ($10^{-8} \sim 10^{-9}$ $m^2 \cdot s^{-1}$ in a condensed phase and $10^{-6} \sim 10^{-7}$ $m^2 \cdot s^{-1}$ in the gaseous state[1,23,59]). At the low temperature limit (≤ 200 K), CO and H_2O have the highest and lowest D_z values, respectively, among the four adsorbates. This reflects the fact that CO is in the gaseous state while H_2O is in a condensed phase at temperatures below 200 K, with diffusivity in the gaseous state being superior to that in a condensed phase. Furthermore, when the temperature was in the high temperature range (≥ 400 K), H_2S had the highest D_z value among the four adsorbates. The D_z value for H_2S at room temperature was calculated at 1.101×10^{-7} $m^2 \cdot s^{-1}$, which corresponds to the results of H_2S in micropore experiments, i.e., $1.02–1.19 \times 10^{-7}$ $m^2 \cdot s^{-1}$, conducted by Chiang *et al.*[60]. At 500 K, all four of the adsorbates are in a gaseous state. The wall's attraction for H_2S and H_2O is much stronger than for CO; therefore, the diffusivity of CO in the direction normal to the pore walls is less pronounced than that of H_2S and H_2O.

Figures 4(a)-(d) show the profiles of distribution density for H_2S, H_2O, CO_2, and CO inside the slit pore with various molar concentrations (0.299 to 3.376 mol/L). The simulations were performed with slit width w = 46.52 Å at room temperature. As shown, each density profile comprises two major and several minor peaks. The strongest peak can be realized as the first adsorption monolayer neighboring the wall. In Fig. 4(a), the density profiles show that both Au(111) and Gr adsorbed significant amounts of H_2S, with Au(111) accommodating more. Due to the effect of oversaturation, excess H_2S molecules spread over the slit space when the concentration exceeded a certain threshold (2.692 mol/L). Please note that the amount of adsorption on each wall increases with the concentration of the adsorbate when the water vapor is in a 'gaseous state'. However, as the density of the water vapor increases, the more densely packed H_2O molecules are not necessarily distributed uniformly within the slit due to the effects of condensation and H-bonding interactions between H_2O molecules. As shown in Fig. 5, this dense collection of H_2O molecules condenses as a liquid-like molecular chain across the slit space with the structure of the chain randomly broken and stochastically adsorbed by either the Au(111) or Gr wall. This mechanism causes irregular changes in the amount of H_2O being adsorbed on the Au(111) and Gr walls. To better comprehend this phenomenon, the transient adsorption conformations and the H-bond distribution state were analyzed by performing the simulation with a high concentration of water vapor (C_m = 3.676 mol/L) inside the slit pore at room temperature. The formation of hydrogen bond can be assessed based on various theoretical and experiment aspects. Here, the geometric criterion was employed to identify the formation of hydrogen bonds. The geometric criterion includes three essential conditions[40], i.e., (i) a bond length between hydrogen and acceptor atoms of less than 2.4 Å, (ii) a distance between the donor and acceptor atoms of less than 3.5 Å, and (iii) a bond angle at the hydrogen atom between the vectors of the hydrogen donor and the hydrogen acceptor of greater than 120°. The atoms illustrated in Fig. 5 are color-coded according to the number of times they were involved in hydrogen bond pairs “at this transient moment”. The blue atoms represent those that are associated with an H-bonded pair. Orange, green, and red atoms denote those involved in two, three, or four H-bonded pairs, respectively. The aggregation of H_2O molecules makes it possible for the formation of a greater number of H-bonds, due to the fact that the oxygen of one H_2O molecule possesses two lone pairs of electrons, each of which can form an H-bond with another H_2O molecule.[61] The duplication of this process means that every H_2O molecule can be H-bonded with up to four other H_2O molecules; i.e., two through its two lone pairs, and two through its two hydrogen atoms.[61] The formation of tangled H-bond networks between H_2O molecules enabled the dense H_2O vapor to condense as a liquid-like molecule chain across the slit space. The structure of the liquid-like molecule chain was time-variant, becoming thinner due to the attractions of the Gr and Au walls. Eventually, the molecule chain was randomly broken and stochastically adsorbed by either the Au(111) or Gr wall, as shown in the inset of Fig. 4(b). This mechanism elucidates the irregular changes of adsorption amounts of H_2O on Au(111) and Gr walls. Note that this unique phenomenon does not occur for pure H_2S because gaseous H_2S molecules lack H-bonds.

Figure 6 shows the changes of D_z value for pure H_2S, CO_2, CO, and H_2O inside the slit as a function of adsorbate concentration at 300 K. The concentration dependence of dynamic diffusivities was determined for molarities of 0.299 to 3.376 mol/L. As shown, the D_z values for each adsorbate decrease with increasing concentration. At a low concentration of 0.299 mol/L, the D_z values of the four adsorbates are quite closed at around $1.256{\sim}1.411 \times 10^{-7}\ m^2{\cdot}s^{-1}$, corresponding to the value of a typical micropore gas[55]. For molarities higher than 1.264 mol/L, H_2O has the lowest D_z values among the four adsorbates. This reflects the fact that H_2O is in a condensed phase while the other three are in the gaseous state at a temperature of 300 K. Moreover, with increasing adsorbate concentration, the D_z values of H_2O and CO_2 decrease more sharply than those of H_2S and CO. This can be ascribed to H_2O and CO_2 tending to coalesce and form large molecular clusters at concentrations above a certain threshold, as shown in Figs. 4(b) and (c).

The slit width greatly affects the adsorption scenario and the adsorption capacity of a microporous adsorbent. Figures 7(a)-(d) show the profiles of distribution probability for H_2S, H_2O, CO_2, and CO inside the slit pore with various widths, ranging from 20.26 to 93.04 Å (to make the insets clear, only w = 23.26 and 93.04 Å are shown for comparison). Simulations were performed with an adsorbate concentration of 1.869 mol/L at 300 K. As shown in Figs. 7(a)-(d), reducing the width of the slit from 93.04 to 23.26 Å distinctly increased the ratio of adsorption. Specifically, when the width of the slit was reduced to 23.26 Å, H_2S, H_2O, and CO_2 completely adsorbed on the walls. This reflects the fact that adsorbates were more affected by the attractions of the walls when the width of the slit was narrowed. Note that the spatial confinement effect also noticeably increased the difference of adsorption ratio between the two walls. For example, in Fig. 7(c), the ratios of CO_2 adsorbed on Gr and Au(111) are 39.9:6.2 for w = 93.04 Å and 96.4:3.6 for w = 23.26

Å. Similar scenarios were found for H_2S, H_2O, and CO adsorption. The results explicitly indicate that adsorbates can be efficiently separated from acidic gas mixtures onto either an Au surface or Gr wall by reducing the slit width.

Figures 8 illustrates changes in diffusivity in the z-direction (D_z) for H_2S, CO_2, CO, and H_2O inside the slit as a function of slit width at 300 K. Simulations were performed with C_m = 1.869 mol/L at various slit widths between 23.26 and 93.04 Å. Due to spatial confinement within the slits, self-diffusivity of each adsorbate in the z direction substantially decreased with a decrease in slit width. In the case of narrow slit pores (w = 23.26 Å), the strong H_2O-Au(111) attractions resulted in H_2O having the highest D_z value among the four adsorbates. As the slit width between the walls was increased ($w \geq$ 46.52 Å), diffusivity in the z-direction was dominated by the adsorbate-adsorbate interactions, in which H_2S and CO have higher D_z values than those of CO_2 and H_2O. This is a clear indication that the gaseous H_2S and CO were highly diffused and dispersing, whereas CO_2 and H_2O tended to coalesce and form dense clusters.

To thoroughly understand the influences of each constituent on the adsorption and separation of acidic gas mixtures, 13 constituent ratios of $H_2S/CO/CO_2/H_2O$ mixtures, listed in Table 7, were assigned in the simulations. The simulations were performed for mixtures with a molar concentration of 1.869 mol/L inside the 46.52-Å slit at room temperature. As shown in Table 7, the mixture with an equimolar fraction of CO_2, H_2O, CO, and H_2S is denoted mixture 1. For the subsequent 12 mixtures, one of the components was reduced in turn by 17.5%, 12.52%, and 6.25%, with the other three components averaged for the remaining fraction. The simulation results of mixture 1 shows that the probabilities of H_2S adsorbed on Au(111) and Gr (i.e., $P_{\mathrm{H2S@Au(111)}}$ and $P_{\mathrm{H2S@Gr}}$) are 69.4% and 30.6%, respectively. Comparing the adsorption results of mixture 1 to those of mixture 4 shows that the ratio of $P_{\mathrm{H2S@Au(111)}}:P_{\mathrm{H2S@Gr}}$ significantly increased from 69.4:30.6 to 80.0:20.0 when the mole fraction of H_2S was reduced from 25% to 6.5%. The ratio of $P_{\mathrm{H2S@Au(111)}}:P_{\mathrm{H2S@Gr}}$ increased from 69.4:30.6 to 77.8:22.2 when H_2O was reduced from 25% to 6.5%. These results show that most of the H_2S constituent can be well separated onto the

Au(111) surface by reducing the constituent ratio of H_2S or H_2O in the mixture.

Figure 9 shows the changes of D_Z values for mixtures with the 13 constituent ratios in Table 7. The simulation results show that the higher the ratio of high-self-diffusivity constituents in the mixture (e.g., H_2S and CO), the higher is the D_Z value of the mixture. For example, As the CO ratio was increased from 6.25% to 25%, the D_Z value of the mixture increased from 8.2 to 9.8 ($\times 10^{-8}$ $m^2 \cdot s^{-1}$). On the other hand, the higher the ratio of low-self-diffusivity constituents in the mixture (e.g., H_2O and CO_2), the lower is the D_Z value of the mixture. For example, when the mole fraction of H_2O was increased from 6.25% to 25%, the D_Z value of the mixture substantially decreased from 11.2 to 9.8 ($\times 10^{-8}$ $m^2 \cdot s^{-1}$). This is because a high ratio of H_2O in the mixture can create more dense H-bonding networks. The H-bonds link the H_2O molecules together, leading to the formation of dense H_2O clusters. These H_2O clusters attracted free CO_2 and H_2S molecules, forming larger carbonic acid structures and hydrates, and therefore decreased the D_Z value of the mixture. To better comprehend the influence of the formation of hydrates and H-bonding networks on adsorption properties, the quantities of H-bonds formed by H_2O-H_2O and H_2S-H_2O interactions, i.e., $N_{H-bond}^{H2O-H2O}$ and $N_{H-bond}^{H2S-H2O}$, for the mixtures with various constituent ratios were evaluated. The results are shown in Table 7. Mixture 10 has the lowest number of H-bonds but the highest D_Z value. The values of $N_{H-bond}^{H2O-H2O}$ distinctly increased with increasing mole fraction of H_2O. However, the values of $N_{H-bond}^{H2S-H2O}$ changed irregularly and relatively less than those of $N_{H-bond}^{H2O-H2O}$. This can be attributed to two factors: (i) the occurance of hydration between H_2O and H_2S is stochastic, and (ii) H_2S has low solubility with water. Note that although H_2S has a molecular structure similar to that of H_2O, H-bonds rarely form between gaseous H_2S molecules because sulphur is insufficiently electronegative for hydrogen bonding.

Figure 10 shows the probabilities of each constituent adsorbed by the Au(111) and Gr walls as a function of temperature. Simulations were performed for mixtures with an equimolar fraction of CO_2, H_2O, CO, and H_2S at a concentration of 3.676 mol/L inside a 46.52-Å slit. The adsorption probabilities shown in Fig. 10 were used to analyze the temperature dependence on the separation of a certain constituent. As shown, at a temperature of 100 K, the probabilities of CO being adsorbed by Au(111) and Gr walls, i.e., $P_{CO@Au}$ and $P_{CO@Gr}$, are 3.7% and 96.3%, respectively. This means that almost all the CO is adsorbed on the Gr wall, with the Au(111) surface remaining three main constituents, i.e., CO_2, H_2O, and H_2S, and a few CO. Similarly, at a temperature of 10 K, the Gr wall adsorbed only H_2S (14.6%), CO_2 (13.9%), and CO (14.3%), without H_2O. Moreover, at a temperature of 200 K, > 95% of CO_2 was adsorbed on the Gr wall, with only H_2S (45.2%), H_2O (30.6%), and CO (17.3%) attached on the Au(111) surface. Of note, when the gas temperature exceeded 400 K, over 80% of H_2S adsorbed on the Au(111) surface. As show in Fig. 10, although the Gr wall lost much of its capability to capture H_2S at the high temperature limit ($\geq$ 400 K), it retained its excellent capacity to adsorb CO_2 in a wide temperature range (200 to 500 K). These tendencies are consistent with adsorption experiments conducted using metal-impregnated carbon sorbents by Cal *et al.*[7]. These results also indicate that the constituents (CO_2, H_2O, CO, and H_2S) in an acidic gas mixture can be well separated by metal/Gr micropore adsorbents by regulating the gas temperature.

Figure 11 shows the probabilities of each constituent being adsorbed by the Au(111) and Gr walls as a function of slit width. Simulations were performed for mixtures with an equimolar fraction of H_2S, H_2O, CO, and CO_2 at a concentration of 3.676 mol/L at 300 K. As shown, each constituent of the mixture adsorbed to the Au(111) and Gr walls at a large slit width (w = 93.04 Å) was commonly in a ratio ranging from 21.3% to 70.0%. Therefore, the effect of constituent separation was indistinct as the slit with a large width. Of note, the separation of constituents became increasingly distinct with decreasing slit width. For a slit width of 23.26 Å, over 90% of CO and CO_2 adsorbed to the Gr surface. The four constituents of the mixture fully separated (CO and CO_2 on the Gr wall and H_2S and H_2O on the Au(111) wall) when the slit width was 11.636 Å. H_2S possesses a dipole moment closer to that of H_2O; therefore, the H_2S is dissolvable in water to become hydrosulfuric acid. The hydrate formation associated with H-bonds between H_2S and H_2O makes the removal of hydrogen sulfide from water troublesome. One effective method for the removal of H_2S from water is to alter the form of the dissolved H_2S by converting it into solid particles via chlorination.[62] The chlorine oxidizes the H_2S, resulting in the formation of insoluble sulfide particles, whereupon activated-carbon filters can be used for the removal of the insoluble sulfide particles as well as residual chlorine from the water.

4. Summary and concluding remarks

The microscopic adsorption mechanism and constituent separation for hydrogen sulfide, oxocarbons, and water vapor mixtures inside metal-doped graphite slits were investigated using MD simulations. The metal addition in the graphitic micropores resulted in two distinct wall materials, i.e., Au and graphite, being simultaneously present in the adsorption system. The difference in adsorption characteristics between the two wall materials led to competitive adsorption, i.e., the two wall materials competed for adsorbates. The competitive adsorption coupled with changes of gas temperature, concentration, constituent ratio, and slit width generated dramatic effects on the separation of multi-component mixtures. For example, the competitive adsorption made constituent separation more distinct with decreasing slit width. For a slit width of 11.6 Å, all the constituents could be completely separated, with H_2S and H_2O adsorbed on the Au(111) surface and CO and CO_2 adsorbed on the Gr wall.

The formation of H-bonding networks and hydrates between H_2O and H_2S molecules also greatly affected the constituent separation of acidic gas mixtures. Simulation results show that the lower the mole fraction of H_2S and H_2O, the better is the separation of H_2S. A high ratio of H_2O and H_2S in mixtures can create more dense H-bonding networks in mixtures. The H-bonds linked H_2O molecules together, leading to the formation of H_2O clusters. These clusters attracted free CO_2 and H_2S molecules, forming larger carbonic acid structures and hydrates, and therefore decreased the self-diffusivities and degraded constituent separation.

When the gas temperature exceeded 400 K, the weak H_2S-Gr interactions could not hold high-kinetic-energy H_2S gases, resulting in over 80% of H_2S adsorbing onto the Au(111) surface. The Au(111) surface has an excellent capability of capturing H_2S but poorly adsorb CO_2 at the high temperature limit ($\geq$ 400 K). This trait is useful for the application of hot gas cleanup in coal gasification process for commercial power plants. Where H_2S must be removed from coal gas to minimize its release into the atmosphere, moreover, it is desirable to remain as much CO_2 as possible since, in high-temperature and pressurized coal gas, carbon dioxide is a valuable working fluid. Moreover, Zn, Ni, Pb and Mn strongly interact with hydrogen sulfide to form insoluble metal sulfides and Pt and Pd are able to adsorb carbon monoxide rapidly. Thus, these metals are viewed as candidate materials for the replacement of noble metal in future research.

Acknowledgements

The author gratefully acknowledges the support provided for this research by the National Science Council of the Republic of China under grants MOST 103-2622-E-020-004-CC3 and MOST 104-2221-E-020-001. I would also like to thank the National Research Program for Biopharmaceuticals (NRPB, NSC 1022325-B-492-001) and the National Center for High-performance Computing (NCHC) of the National Applied Research Laboratories (NARLabs) of Taiwan for providing computational and storage resources.

References

[1] Y. Xiao, S. Wang, D. Wu and Q. Yuan, *J. Hazard. Mater.*, 2008, **153**, 1193–1200.

[2] T. D. Burchell, R. R. Judkins, M. R. Rogers and A. M. Williams, *Carbon*, 1997, **35**, 1279–1294.

[3] R. Quinn and D. V. Laciak, *J. Membrane. Sci.*, 1997, **131**, 49–60.

[4] P. Forzatti and L. Lietti, *Catal. Today*, 1999, **52**, 165–181.

[5] Y. Xiao, S. Wang, D. Wu and Q. Yuan, *Sep. Purif. Technol.*, 2008, **59**, Issue 3, 326–332.

[6] L. W. Tsay, M. Y. Chi, H. R. Chen and C. Chen, *Mat. Sci. Eng. A-Struct.*, 2006, **416**, 155–160.

[7] M. P. Cal , B. W. Strickler and A. A. Lizzio, *Carbon*, 2000, **38**, 1757–1765.

[8] B. Kvamme, T. Kuznetsova and K. Aasoldsen, *J. Mol. Graph. Model.*, 2005, **23**, 524–536.

[9] V. Buch, J. Paul Devlin, I. A. Monreal, B. J. Cwiklik and N. U. Aytemiz, *Phys. Chem. Chem. Phys.*, 2009, **11**, 10245–10265.

[10] J. Lindenmann, V. Matzi, N. Neuboeck, B. Ratzenhofer-Komenda, A. Maier and F. M. Smolle-Juettner, *Diving Hyperb. Med.*, 2010, **40**(4), 213–7.

[11] E. Lowicka and J. Beltowski, *Pharmacol. Rep.*, 2007, **59**, 4–24, and therein.

[12] B. H. Tan, P. T. H. Wong and J. S. Bian, *Neurochem. Int.*, 2010, **56**,3–10, and therein.

[13] G. Shang, G. Shen, T. Wang and Q. Chen, *J. Air Waste. Manage. Assoc.*, 2012, **62**(8), 873–879.

[14] A. J. Leavitt and T. P. Beebe, Jr., *Surf. Sci.*, 1994, **314**, 23–33.

[15] F. Faure, B. Rousseau, V. Lachet and P. Ungerer, *Fluid. Phase. Equilibr.*, 2007, **261**, 168–175.

[16] R. Hellmann, E. Bich, E. Vogel and V. Vesovic, *Phys. Chem. Chem. Phys.*, 2011, **13**, 13749–13758.

[17] H. Sellers, *Surf. Sci.*, 1993, **294**, 99–107.

[18] J. Vorholz, B. Rumpfz and G. Maurer, *Phys. Chem. Chem. Phys.*, 2002, **4**, 4449–4457.

[19] Y. H. Zhang, Y. B. Chen, K. G. Zhou, C. H. Liu, J. Zeng, H. L. Zhang and Y. Peng, *Nanotechnology*, 2009, **20**, 185504.

[20] D. Britt, D. Tranchemontagne and O. M. Yaghi, *Proc. Natl. Acad. Sci. U. S. A.* 2008, **105**, 11623-11627.

[21] R. Lu, Z. Meng, D. Rao, Y. Wang, Q. Shi, Y. Zhang, E. Kan, C. Xiao and K. Deng, *Nanoscale*, 2014, **6**, 9960-9964.

[22] S. E. Nam and K. H. Lee, *J. Membrane. Sci.*, 2001, **192**, 177–185.

[23] P. H. Huang, S. C. Hung and M. Y. Huang, *Phys. Chem. Chem. Phys.*, 2014, **16**, 15289–15298.

[24] Y. C. Yortsos and A. K. Stubos, *Curr. Opin. Colloid Interface Sci.*, 2001, **6**, 208–216.

[25] R. Evans, U. M. B. Marconi and P. Tarazona, *J. Chem. Soc., Faraday Trans. 2*, 1986, **82**, 1763–1787.

[26] Z. A. Makrodimitri, D. J. M. Unruh and I. G. Economou, *J. Phys. Chem. B*, 2011, **115**, 1429–1439.

[27] A. Vishnyakov, P. I. Ravikovitch and A. V. Neimark, *Langmuir*, 1999, **15**, 8736–8742

[28] A. Kapoor and R. T. Yang, *Chem. Eng. Sci.*, 1989, **44**, 1727–1733.

[29] C. Pelekani and V. L. Snoeyink, *Wat. Res.*, 1999, **33**, 1209–1219.

[30] Y. C. Wang and S. P. Ju, *Phys. Chem. Chem. Phys.*, 2011, **13**, 1323–1331.

[31] B. Collignon and S. Picaud, *Chem. Phys. Lett.*, 2004, **393**, 457–463.

[32] Z. Chang, D. S. Zhang, Q. Chen and X. H. Bu, *Phys. Chem. Chem. Phys.*, 2013, **15**, 5430.

[33] P. H. Huang, J. W. Jhan, Y. M. Cheng and H. H. Cheng, *Sci. World J.*, 2014, **2014**, 937867.

[34] P. H. Huang, H. H. Cheng and S. H. Lin, *E-J. Chem.*, 2015, **2015**, 106590.

[35] Z. Li, Y. Wang, A. Kozbial, G. Shenoy, F. Zhou, R. McGinley, P. Ireland, B. Morganstein, A. Kunkel, S. P. Surwade, L. Li and H. Liu, *Nat. Mater.*, 2013, **12**, 925–931.

[36] T. Werder, J. H. Walther, R. L. Jaffe, T. Halicioglu and P. Koumoutsakos, *J.*

Phys. Chem. B, 2003, **107**, 1345–1352.

[37] J. J. Magda, M. Tirrell and H. T. Davis, *J. Chem. Phys.*, 1985, **83**, 1888–1901.

[38] H. M. Williams, E. A. Dawson, P. A. Barnes, G. M. B. Parkes and L. A. Pears, *J. Porous. Mater.*, 2009, **16(5)**, 557-564.

[39] V. Kumar, N. Talreja, D. Deva, N. Sankararamakrishnan, A. Sharma and N. Verma, *Desalination*, 2011, **282**, 27–38.

[40] M. Levitt, M. Hirshberg, R. Sharon and V. Daggett, *Comput. Phys. Commun.*, 1995, **91**, 215–231.

[41] M. Levitt, M. Hirshberg, R. Sharon, K. E. Laidig and V. Daggett, *J. Phys. Chem. B,* 1997, **101***,* 5051–5061.

[42] E. Spohr, *J. Electroanal. Chem.,* 1998, **450**, 327.

[43] Y. Dou, L. V. Zhigilei, N. Winograd and B. J. Garrison, *J. Phys. Chem. A*, 2001, **105**, 2748.

[44] S. L. Mayo, B. D. Olafson and W. A. Goddard, *J. Phys. Chem.,* 1990, **94**, 8897.

[45] S. S. Jang, Y. H. Jang, Y. H. Kim, W. A. Goddard, A. H. Flood, B. W. Laursen, H. R. Tseng, J. F. Stoddart, J. O. Jeppesen, J. W. Choi, D. W. Steuerman, E. Delonno and J. R. Heath, *J. Am. Chem. Soc.,* 2005, **127**, 1563.

[46] A. V. Shevade, S. Jiang and K. E. Gubbins, *J. Chem. Phys.*, 2000, **113**, 6933.

[47] S. Pałucha, Z. Gburski and J. Biesiada, *J. Mol. Struct.*, 2004, **704**, 269–273.

[48] A. Alexiadis and S. Kassinos, *Chem. Phys. Lett.*, 2008, **460**, 512–516.

[49] S. K. Nath, *J. Phys. Chem. B*, 2003, **107** (35), 9498–9504.

[50] W. L. Jorgensen, J. Chandrasekhar, J. D. Madura, E. W. Impey and M. L. Klein, *J. Chem. Phys*., 1983, **79**, 926-935.

[51] B. D. Kay, K. R. Lykke, J. R. Creighton and S. J. Ward, *J. Chem. Phys.*, 1989, **91**, 5120.

[52] J. M. Haile, *Molecular dynamics simulation: elementary methods*, Wiley-Interscience, New York, 1997.

[53] P. H. Huang, *Mater. Chem. Phys.*, 2011, **131**, 297.

[54] J. K. Kuo, P. H. Huang, W. T. Wu and C. M. Lu, *Appl. Phys. A.*, 2014, **114**, 1247–1256.

[55] B. Hammer, Y. Morikawa and J. K. Nørskov, *J. Phys. Chem. B*, 2006, **110**, 17512–17517.

[56] M. Rubes, J. Kysilka, P. Nachtigall and O. Bludsky, *Phys. Chem. Chem. Phys.,* 2010, **12**, 6438–6444.

[57] G. Vidali, G. Ihm, H. Y. Kim and M. W. Cole, *Surf. Sci. Rep.,* 1991, **12**, 135.

[58] B. Hammer and J. Norskov, *Nature* 1995, **376**, 238-240.

[59] M. Holz, S. R. Heil and A. Sacco, *Phys. Chem. Chem. Phys.*, 2000, **2**, 4740–4742.

[60] H. L. Chiang, J. H. Tsai, D. H. Chang and F. T. Jeng, *Chemosphere,* 2000, **41**, 1227–1232.

[61] A. Rastogi, A. K. Ghosh and S. J. Suresh, Thermodynamics- Physical Chemistry of Aqueous Systems, J. C. Moreno-Piraján (Ed.), 2011, ISBN: 978-953-307-979-0. InTech.

[62] L. Zhang, P. D. Schryver, B. D. Gusseme, W. D. Muynck, N. Boon and W. Verstraete, *Water Res*., 2008, **42**, 1-12.

Tables

Table 1 ENCAD parameters[40,41] of bond length energy and bond angle energy used for H_2O, CO_2, CO, and H_2S molecules.

Parameter (units)	k_b^i (kcal·mol^{-1}Å^{-2})	b_0^i (Å)	k_θ^i (kcal·mol^{-1}rad^{-2})	θ_0^i (deg)
$(O\text{-}H)_{H_2O}$	250	1.0	60	109.47
$(C\text{-}O)_{CO_2}$	5000	1.163	5000	180
$(C\text{-}O)_{CO}$	5000	1.128	–	–
$(S\text{-}H)_{H_2S}$	250	1.336	60	92.1

Table 2 Energy parameters of F3C model[41] used for water molecular interactions.

Parameter	r_0 (Å)	ε (kcal/mol)	q (e)
O_{H_2O}	3.55322	0.18479	-0.82
H_{H_2O}	0.9	0.01	0.41

Table 3 Intermolecular energy parameters for L-J and Coulomb interactions.

Parameter	r_0 (Å)	ε (kJ/mol)	q (e)
C_{Gr}[46]	3.4	0.2328	0
H_{H_2O}[36]	2.24	0.2750	0.41
O_{H_2O}[36]	2.98	0.6567	-0.82
C_{CO}[47]	3.55	0.3089	0.0223
O_{CO}[47]	2.95	0.512	-0.0223
C_{CO_2}[48]	2.7918	0.23982	0.5888
O_{CO_2}[48]	3.0	0.68722	-0.2944
S_{H_2S}[49]	3.72	2.0785	-0.248
H_{H_2S}[49]	0.98	0.03243	0.124

Table 4 Au-H_2O interaction parameters in modified Spohr potential energy function.[43]

D_0 (eV)	β_O (Å^{-1})	β_H (Å^{-1})	r_{e1} (Å)	r_{e2} (Å)	λ	R_{on} (Å)	R_{off} (Å)
0.0668	1.30	1.30	3.70	-1.0	0.2	7.0	11.0

Table 5 Potential parameters in Dreading force field.

Parameter	*D* (kcal/mol)	R (Å)	*z*
Au-C[45]	0.064	3.561	12
Au-H[45]	0.041	3.082	12
Au-O[45]	0.048	3.395	12
Au-S	1.892	2.885	12

Table 6. Binding energy (E_b) and mean equilibrium distance (r_e) for H_2S, CO_2, CO, and H_2O molecules on Au(111) and Gr surfaces obtained in this study and from other works.

	adsorbed on Au(111)		adsorbed on Gr	
	$\lvert E_b \rvert$ (kJ/mol)	r_e (Å)	$\lvert E_b \rvert$ (kJ/mol)	r_e (Å)
H_2S	40.06, 41.02^a, 39.35^b	2.338	14.30	3.535
H_2O	44.54, 43.89^c	3.035	11.69, 13.0^e	3.07, 3.19^e
CO	3.24, 3.859^d	2.954	10.14, 10.73^e, 10.6^f	3.33, 3.23^e
CO_2	4.39	2.931	16.57, 16.47^e, 17.2^f	3.16, 3.14^e, 3.2^f

$^{a,\ c,\ f}$: obtained from experiments cited in Refs. 14, 51, and 57, respectively. $^{b,\ d}$: obtained from ab initio calculations cited in Refs. 17 and 55, respectively. ^{e}: obtained using density functional theory/coupled cluster method in Ref. 56.

Table 7. Various component ratios of mixtures used in simulations. $P_{\mathrm{H2S@Au(111)}}$ and $P_{\mathrm{H2S@Gr}}$ denote probabilities of H_2S adsorbed on Au(111) and Gr surfaces, respectively. $N_{H-bond}^{H2O-H2O}$ and $N_{H-bond}^{H2S-H2O}$ are numbers of H-bonds formed by H_2O-H_2O and H_2S-H_2O interactions, respectively.

Composition	CO_2(%)	H_2O(%)	CO(%)	H_2S(%)	$P_{\mathrm{H2S@Au(111)}}$(%)	$P_{\mathrm{H2S@Gr}}$(%)	$N_{H-bond}^{H2O-H2O}$	$N_{H-bond}^{H2S-H2O}$
mixture 1	25	25	25	25	69.44	30.56	215	19
mixture 2	27.5	27.5	27.5	**17.5**	72.22	27.78	238	15
mixture 3	29.16	29.16	29.16	**12.52**	62.22	37.78	267	10
mixture 4	31.25	31.25	31.25	**6.25**	80.00	20.00	279	10
mixture 5	27.5	27.5	**17.5**	27.5	67.67	32.33	242	27
mixture 6	29.16	29.16	**12.52**	29.16	70.95	29.05	259	23
mixture 7	31.25	31.25	**6.25**	31.25	72.44	27.56	268	18
mixture 8	27.5	**17.5**	27.5	27.5	72.73	27.27	136	15
mixture 9	29.16	**12.52**	29.16	29.16	73.90	26.10	86	22
mixture 10	31.25	**6.25**	31.25	31.25	77.78	22.22	39	18
mixture 11	**17.5**	27.5	27.5	27.5	74.75	25.25	236	18
mixture 12	**12.52**	29.16	29.16	29.16	67.62	32.38	269	19
mixture 13	**6.25**	31.25	31.25	31.25	62.22	37.78	286	25

Figures

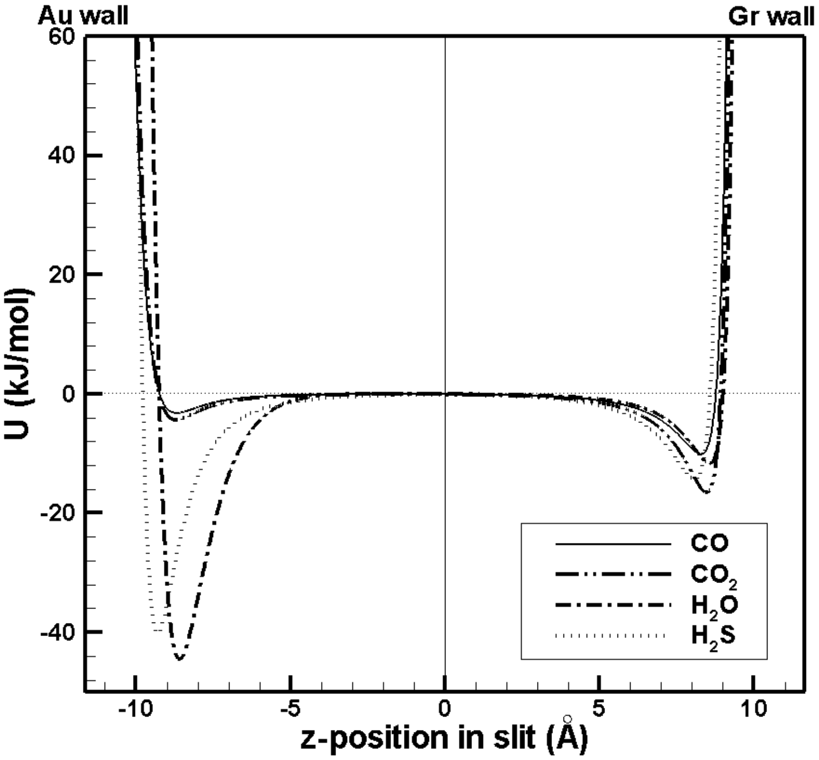

FIG. 1. Interaction energy between various adsorbate molecules and Au(111)/Gr slit pore as function of molecular position in slit. Slit width is 23.26 Å.

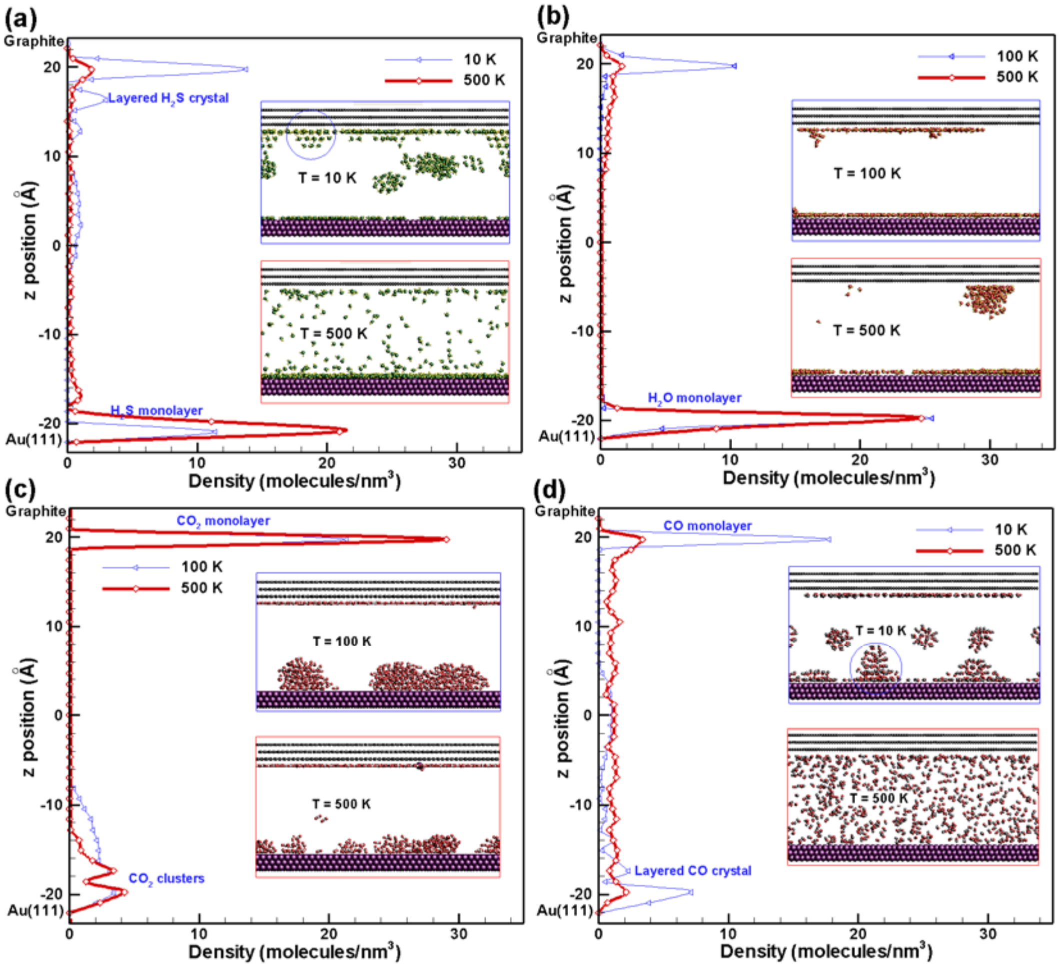

FIG. 2. Profiles of local distribution density for (a) H_2S, (b) H_2O, (c) CO_2, and (d) CO molecules inside Au(111)/Gr slit pore at various temperatures. Simulations were performed with C_m = 1.869 mol/L and w = 46.52 Å. Insets show corresponding adsorption conformations.

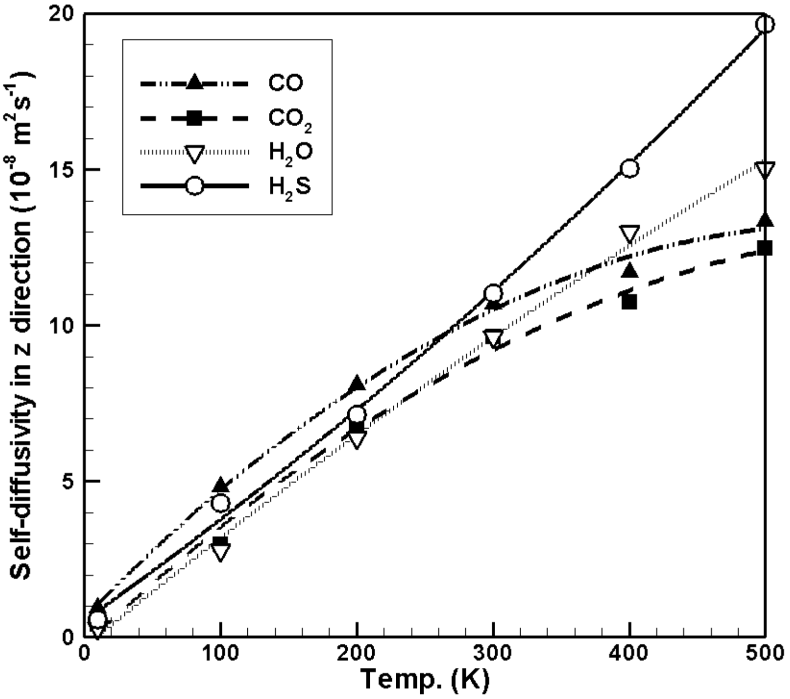

FIG. 3. Self-diffusivity in z direction as function of temperature for pure H_2S, CO_2, CO, and H_2O molecules inside slit pore. Simulations were performed with C_m = 1.869 mol/L and w = 46.52 Å.

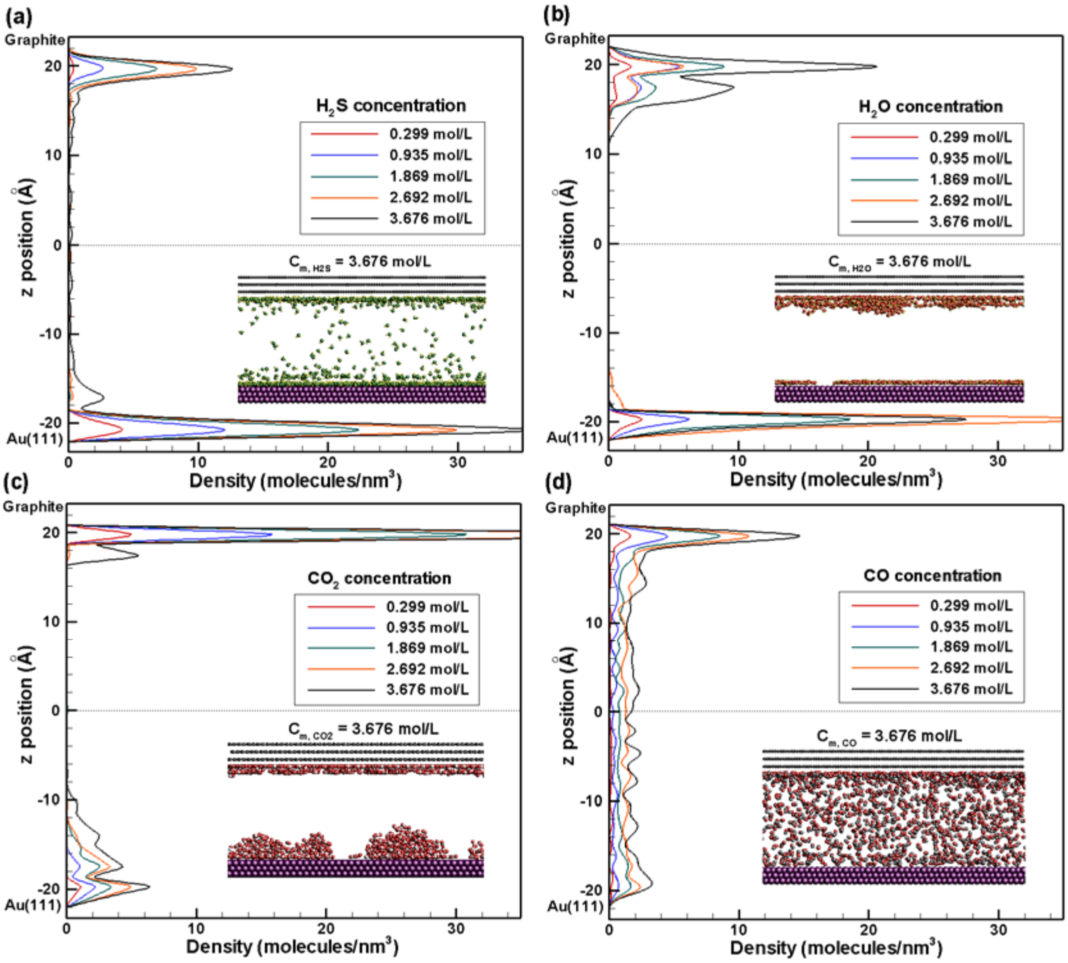

FIG. 4. Profiles of distribution density for (a) H_2S, (b) H_2O, (c) CO, and (d) CO_2 molecules inside slit pore at various concentrations. Simulations were performed with w = 46.52 Å at 300 K. Insets show corresponding adsorption conformations.

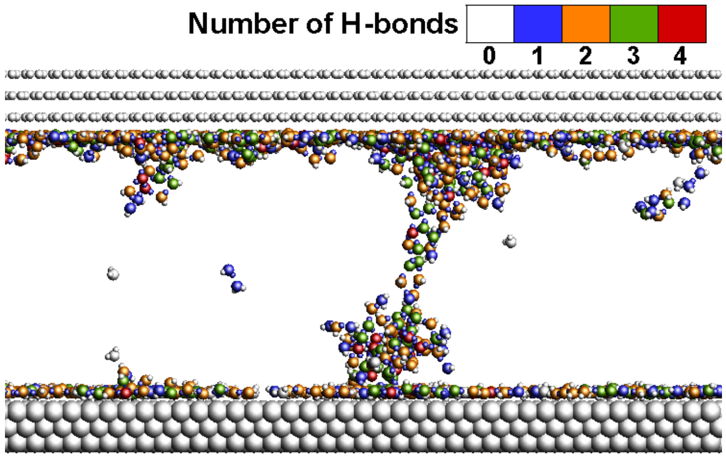

FIG. 5. Transient adsorption conformations of water vapor at high concentration (C_m = 3.676 mol/L) inside Au(111)/Gr slit pore with w = 46.52 Å at room temperature. Atoms are color-coded according to the number of times they were involved in hydrogen bond pairing “at this transient moment”.

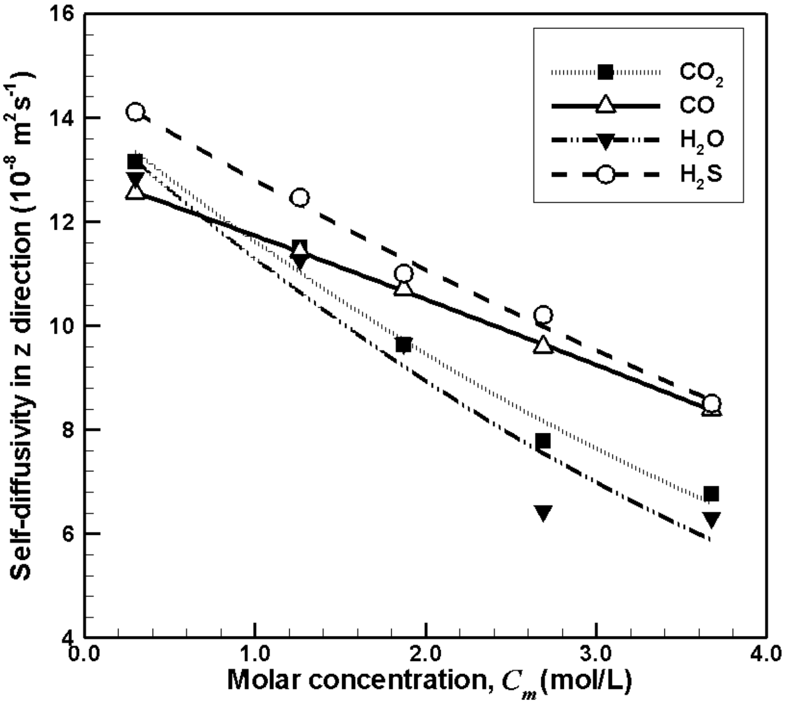

FIG. 6. Self-diffusivity in z direction as function of adsorbate concentration for pure H_2S, CO_2, CO, and H_2O molecules. Simulations were performed with w = 46.52 Å at room temperature.

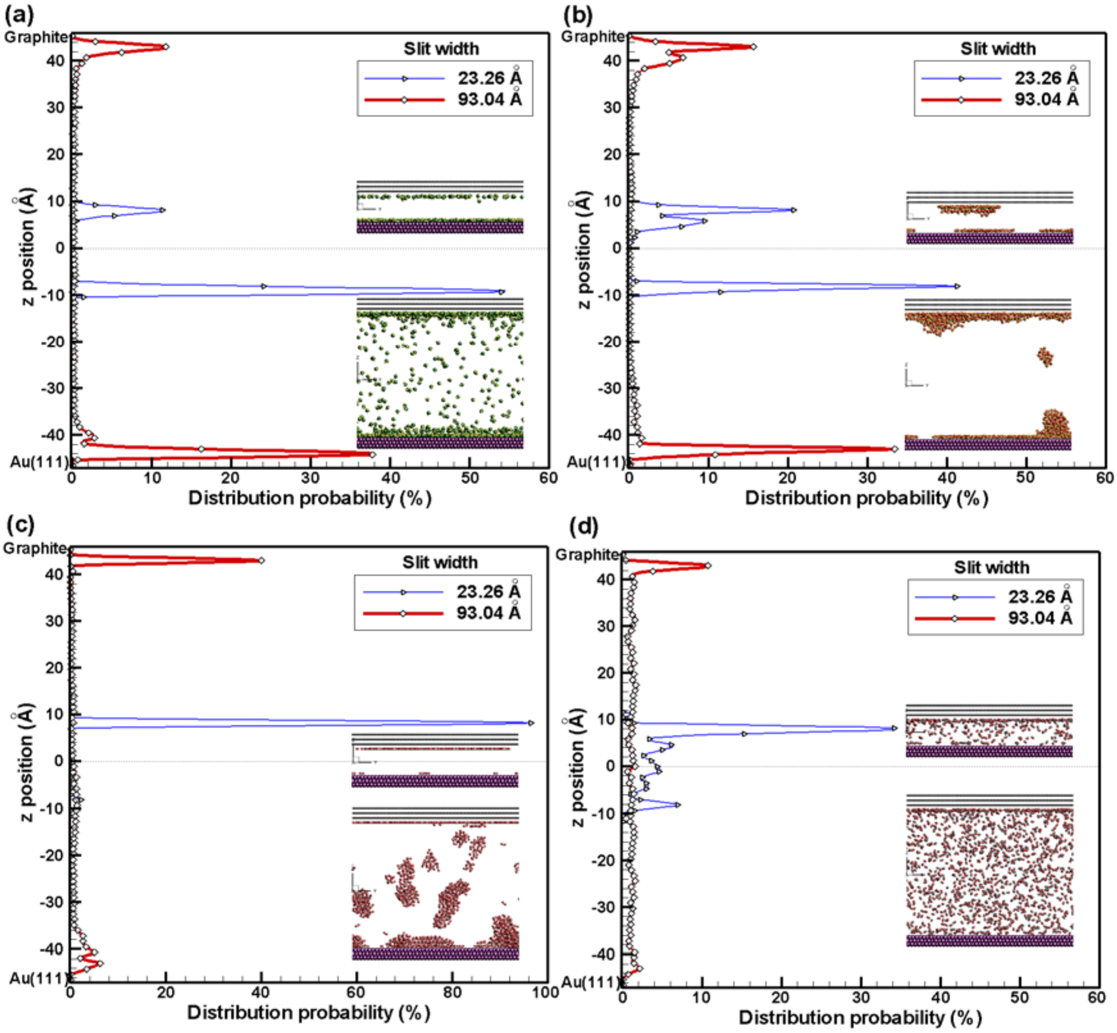

FIG. 7. Profiles of distribution probability for (a) H_2S, (b) H_2O, (c) CO_2, and (d) CO molecules inside slit pore at various slit widths (only w = 23.26 and 93.04 Å are shown). Simulations were performed with C_m = 1.869 mol/L at 300 K. Insets show corresponding adsorption conformations.

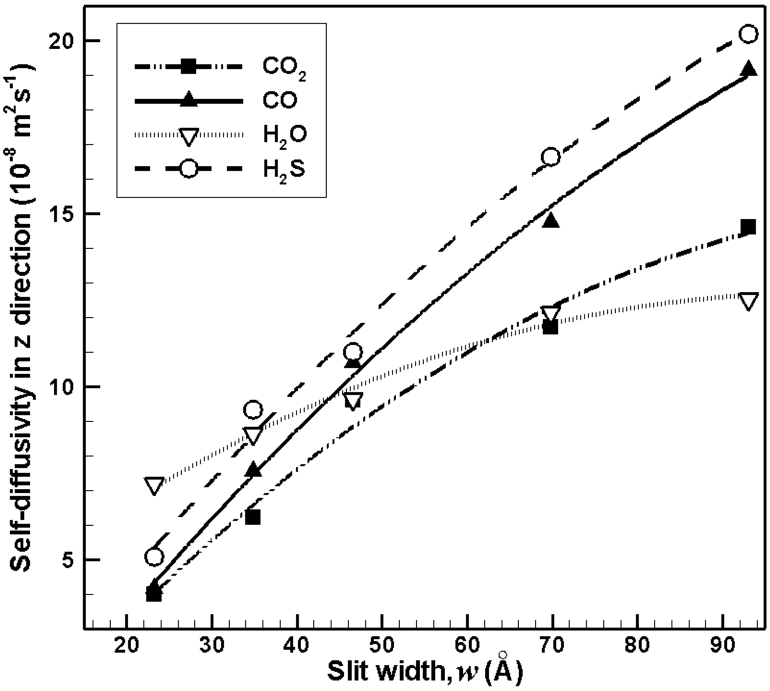

FIG. 8. Self-diffusivity in *z* direction as function of slit width for pure H_2S, CO_2, CO, and H_2O molecules. Simulations were performed with C_m = 1.869 mol/L at room temperature.

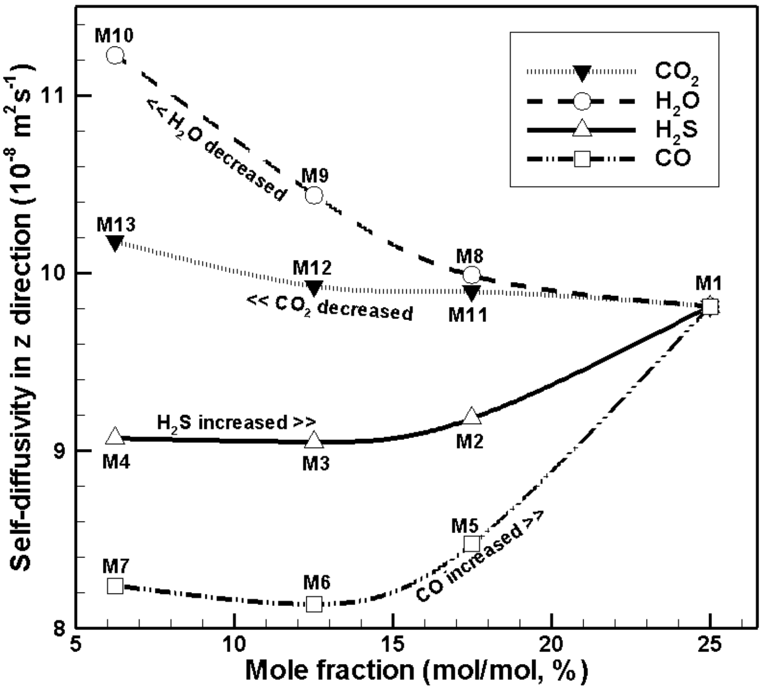

FIG. 9. Changes of D_Z value as function of mole fraction for mixtures with various constituent ratios at 300 K. Labels M1, M2,…, M13 correspond to constituent ratios of mixtures 1 to 13, respectively, in Table 7 (e.g., M1 denotes the mixture of CO_2:H_2O:CO:H_2S with equimolar fraction (25%:25%:25%:25%), and M2 denotes that with 27.5%:27.5%:27.5%:17.5%). Lines show changes of self-diffusivity with changing concentration of a certain component.

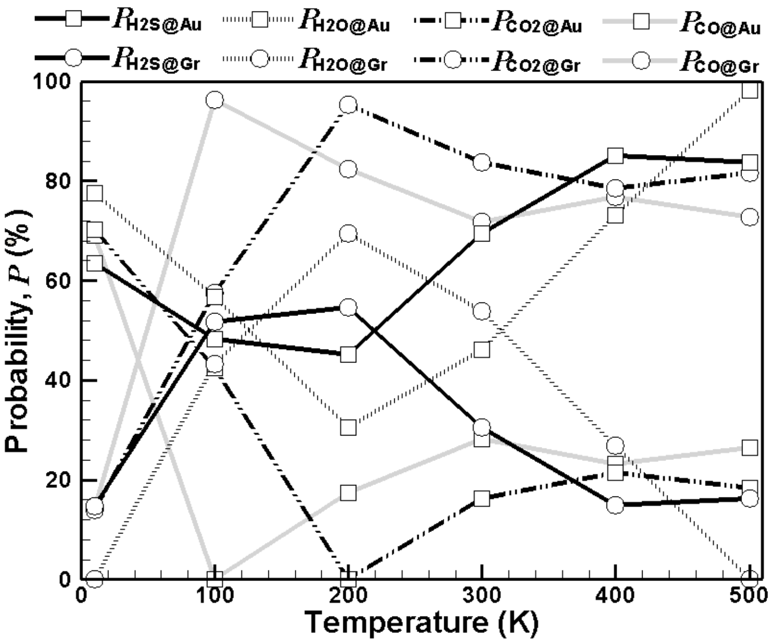

FIG. 10. Probabilities for each constituent adsorbed by Au(111) and Gr walls as function of temperature. Simulations were performed for mixtures with equimolar fraction of CO_2, H_2O, CO, and H_2S at concentration of 3.676 mol/L inside 46.52-Å slit.

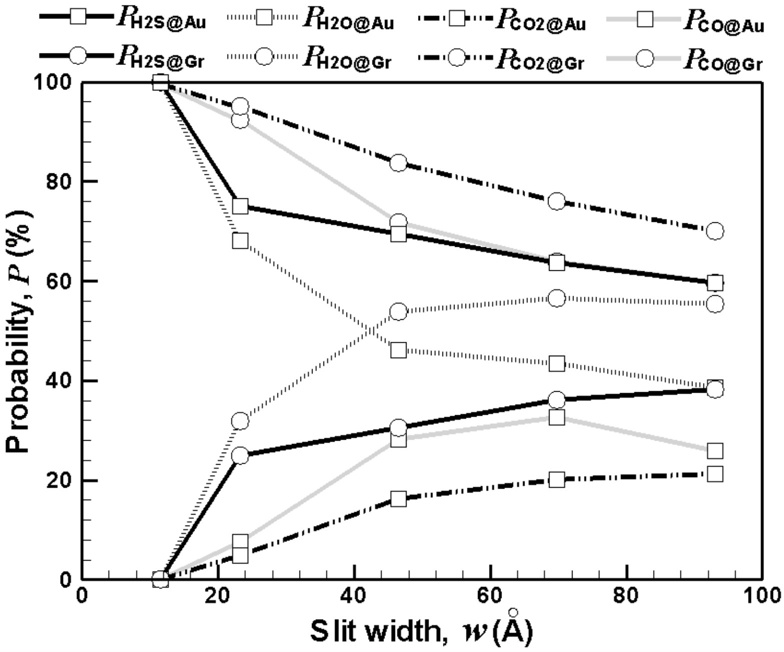

FIG. 11. Probabilities for each constituent adsorbed on Au(111) and Gr surfaces as function of slit width. Simulations were performed for mixtures comprising equimolar fraction of CO_2, H_2O, CO, and H_2S at concentration of 3.676 mol/L at 300 K.